

Prediction of photothermal phase signatures from arbitrary plasmonic nanoparticles and experimental verification

Omry Blum and Natan T. Shaked*

Department of Biomedical Engineering, Faculty of Engineering, Tel Aviv 69978, Israel.

*nshaked@tau.ac.il

We present a new approach for predicting spatial phase signals originated from photothermally excited metallic nanoparticles of arbitrary shapes and sizes. Heat emitted from the nanoparticle affects the measured phase signal via both the nanoparticle surrounding refractive index and thickness changes. Since these particles can be bio-functionalized to bind certain biological cell components, they can be used for biomedical imaging with molecular specificity, as new nanoscopy labels, and for photothermal therapy. Predicting the ideal nanoparticle parameters requires a model that computes the thermal and phase distributions around the particle, enabling more efficient phase imaging of plasmonic nanoparticles, and sparing trial and error experiments of using unsuitable nanoparticles. For the first time to our knowledge, using the proposed model, one can predict phase signatures from nanoparticles with arbitrary parameters. The proposed nonlinear model is based on a finite-volume method for geometry discretization, and an implicit backward Euler method for solving the transient inhomogeneous heat equation. To validate the model, we correlate its results with experimental results obtained for gold nanorods of various concentrations, which we acquired by a custom-built wide-field interferometric phase microscopy system.

Keywords: *interferometric imaging; digital holographic microscopy; phase measurement; nanoparticles; plasmonics*

INTRODUCTION

Plasmonic nanoparticles are incorporated in a variety of scientific disciplines due to their unique interactions with electromagnetic fields. Plasmonic nanoparticles are used in photonics to sense or impose change in a certain environment, acting as nanosensors for chemical, thermal or material property changes.¹ In biomedical applications, plasmonic nanoparticles can be used as labels in cells and tissues and are imaged via various effects, including photothermal (PT) imaging, photoacoustic shock-wave imaging, and polarization imaging.²⁻⁵

Electromagnetic energy absorbed by a metallic nanoparticle quickly transforms into heat due to electron-phonon relaxation; thus, nanoparticles placed in solution act as nano-sources of heat, which can be manipulated for imaging or for destructive purposes.

Several numerical models of nanoparticles have estimated the transference of heat from a nanoparticle submerged in liquid to its surrounding.⁵⁻⁸ These models can yield information on the processes nanoparticles undergo in time scales or resolutions smaller than it is possible to measure. In addition, these models can predict the thermal distribution in the nanoparticle surrounding, making it possible to explain phenomena seen when

heated particles interact with other materials, in particular with biological materials that are prone to thermal damage.

By conjugating the nanoparticles to biological carriers such as antigens, they can attach to the appropriate biological cell receptors and molecularly specific excitation of these nanoparticles by light can be accomplished.^{9,10} Due to the connection between the local temperature change in the solution surrounding the nanoparticle and the phase of light interacted with the solution, imaging the nanoparticles and detecting their locations are possible. Hence, imaging the nanoparticles as heat sources can be implemented with phase-sensitive techniques such as differential interference contrast microscopy,^{11,12} phase-sensitive optical coherence microscopy,^{13,14} and wide-field interferometric phase microscopy.¹⁵ In these PT phase imaging methods, the nanoparticles are stimulated at their peak plasmonic wavelength by a time-modulated illumination. The nanoparticle optical excitation induces absorption, yielding temperature rise in the nanoparticle surroundings, which causes phase changes that can be detected optically.

Optimization and enhancement of the nanoparticle phase signal is expected to improve imaging capabilities of these phase-sensitive techniques. This can be conducted by a careful design of

the nanoparticle material, shape and size, which greatly affect its optical properties and the resulting phase signal. Instead of synthesizing many types of nanoparticles and trying them experimentally, simulation tools for prior evaluation of the expected thermal and phase signals can be used. Only after simulative inspection and optimization of the nanoparticles, the experimental synthesis of the chosen nanoparticles should be carried out. However, to the best of our knowledge, currently there is no study that simulates the optical quantitative phase profiles extracted from heated nanoparticles of arbitrary shapes, directed at optimization of the nanoparticle shape and size and the related optical phase imaging system parameters, and allowing optimization of nanoparticles for a certain need; for example, to form the strongest phase signal possible for phase imaging without yielding damaging temperature rise, or, alternatively, for obtaining the highest temperature possible for PT therapy.

This paper suggests a computational model that predicts the quantitative phase profiles of photothermally-excited plasmonic nanoparticles of arbitrary shapes. The model is based on finite-volume method for geometry discretization, and an implicit backward Euler method for solving the transient inhomogeneous heat equation. The local heat change is then related to the phase change via both the refractive index and thickness changes. Experimental validation of the model is carried out by wide-field phase imaging of gold nanorods using an interferometric microscopy system.

MATERIALS AND METHODS

Heat Model

Our heat model assumes that small solid particles with high surface to volume ratio, which are situated within a liquid medium, experience strong frictional forces causing them to quickly minimize their speed relative to the medium. This behavior is relevant for nanoparticles suspended in fluid, and as such, they remain stationary within their surrounding medium during measurement time. Heat transfer by convection occurs due to relative movement of two adjacent materials, from which we deduce that omission of heat transfer by convection in this model is acceptable. For simplicity, we assume that the nanoparticles do not occlude each other and do not aggregate. Otherwise, both their cross-section and spectral absorption might be changed.

Biological tissue is sensitive to temperature change. Temperature rise of more than 5 °C above homeostasis causes tissue damage over time.¹⁶ Laser-induced short and powerful pulses during a few nanoseconds, with energy of as low as 1 mJ, can cause tissue damage due to heat buildup.¹⁷ Temperature rise on the nanoparticle surface of above 100 °C involves water vaporization. When thermally stimulating a nanoparticle suspended in water solution to excessive temperatures, vapor bubble may form around the nanoparticle, which changes the surrounding material dielectric constant, as well as the nanoparticle extinction and absorption coefficients.¹⁸ This vapor formation may cause strong cavitation and pressure waves that damage the surrounding tissue. Heat transfer model of spherical nanoparticles considering these effects was discussed previously.⁷ Our model, however, avoids these cases, and assumes that the temperature of the thermally stimulated nanoparticles suspended in medium does not exceed 100 °C, and thus vapor formation is

negligible. Due to lack of vapor layer, we assume boundary-free surrounding around the nanoparticles, yielding uniform temperature and energy flux at the particle-medium boundary.

In addition, we assume that the absorption coefficient and the cross-section of the nanoparticle are known for all wavelengths. We can then assume excitation of the particle in its peak absorption wavelength, causing surface plasmon resonance (SPR).

As mentioned above, since we assume that convection heat transfer is negligible at the nanoscale, conduction governs the thermal distribution problem. When incorporating many identical heat sources, one can first find the thermal distribution solution for a single source, and then use superposition to derive the collective solution. Since the proposed model was designed mainly for phase investigation originating from photothermally stimulated nanoparticles, we finally used transition from heat to the accumulated phase.

We chose the finite-volume method for discretization with a grid containing n^3 Cartesian cubic voxels with constant volume. This method is particularly accurate for energy conservation equations, such as the heat equation.¹⁹

Under these conditions, the transient inhomogeneous, internal-heat-generation, conduction-only heat equation is:

$$\rho C_p \frac{\partial T}{\partial t} = \kappa \nabla^2 T + S, \quad (1)$$

where ρ is material (i.e. water/gold) density [kg/m^3], C_p is the material specific heat at constant pressure [$\text{J} \times (\text{°K} \times \text{kg})^{-1}$], T is the material temperature [°K], κ is the material thermal conductivity [$\text{W} \times (\text{°K} \times \text{m})^{-1}$], ∇^2 is the Laplace operator, which equals to $\partial^2 T / \partial x^2 + \partial^2 T / \partial y^2 + \partial^2 T / \partial z^2$ in Cartesian coordinates, and S is the generated heat term due to laser excitation [W/m^3]. This equation operates within two regions, the nanoparticle region and the medium region. Each region has its own coefficients for material density ρ , specific-heat C_p , thermal conductivity κ , and heat generation S . In the nanoparticle region, S is calculated from the energy absorbed by the particle in accordance with its cross-section. This parameter is calculated as follows:

$$S = (I \times C) / (A \times V), \quad (2)$$

where I is the excitation laser intensity [W], A is the excitation laser spot area [m^2], C is the particle optical cross-section [m^2], and V is the particle volume [m^3]. The particle optical cross-section can be calculated by either an analytical method, if possible, such as the Mie theory, or by a numerical method, such as the discrete dipole approximation. In the surrounding medium region, S is considered zero; thus we assume that direct medium heating due to laser illumination is negligible.

Analytical solutions for Eq. (1) may be derived with great effort only for highly symmetric shapes. Numerical methods, on the other hand, can be applied to solve this equation for arbitrary shapes, non-uniform media, and time-changing heat-source terms. In general, numerical methods for solving the heat equation can be divided into explicit and implicit methods. In explicit methods, the solution for the next time step is derived straightforward from the present time step; whereas in implicit methods, the solution for the next time step is derived by solving a system of equations built from the present time step, connecting all elements on grid to the next time step solution. In our model, we use an implicit backward-Euler method to solve the heat equation.¹⁹ Since we use time-

modulated PT illumination to stimulate the nanoparticles, we have an oscillating time-dependent heat-source term S . Derivation of temperature is discretized in space using three-point, second-order central difference, which adds a truncation error of $O(h)$, where h is the characteristic size of a voxel.²⁰ In this case, for each voxel located at $r = (x, y, z)$, the product of κ by the Laplace operator in Eq. (1) can be rewritten as a linear combination of its neighboring voxels, as follows:

$$\begin{aligned} \kappa \nabla_r^2 T = \frac{1}{h^2} & [\kappa_{x+0.5,y,z}(T_{x+1,y,z} - T_{x,y,z}) + \\ & \kappa_{x-0.5,y,z}(T_{x-1,y,z} - T_{x,y,z}) + \\ & \kappa_{x,y+0.5,z}(T_{x,y+1,z} - T_{x,y,z}) + \\ & \kappa_{x,y-0.5,z}(T_{x,y-1,z} - T_{x,y,z}) + \\ & \kappa_{x,y,z+0.5}(T_{x,y,z+1} - T_{x,y,z}) + \\ & \kappa_{x,y,z-0.5}(T_{x,y,z-1} - T_{x,y,z})]. \end{aligned} \quad (3)$$

The thermal conductivity might change per location on the grid, since it depends upon the materials modeled. As such, in Eq. (3) we used the thermal conductivities at the borders between two voxels, where each voxel has six borders and the conductivities there are determined by harmonic average of the corresponding neighboring voxel conductivities, for complying with conservation of energy law. For example:

$$\kappa_{x+0.5,y,z} = 2\kappa_{x,y,z}\kappa_{x+1,y,z}/(\kappa_{x,y,z} + \kappa_{x+1,y,z}). \quad (4)$$

At infinity, we assume constant temperature, and thus discretized boundary condition at edges of the grid is set to $T = 25^\circ\text{C}$.

For each voxel located at (x, y, z) , we can further discretize Eq. (1) according to backward-Euler method, as follows:

$$\begin{aligned} \rho C_p \frac{(T_{x,y,z;n+1} - T_{x,y,z;n})}{dt} = \\ \kappa \cdot (\nabla_{r;n+1}^2 T) + S, \end{aligned} \quad (5)$$

where n and $n+1$ represent two successive time points. Reorganization of Eq. (5) produces the following equation:

$$\begin{aligned} \rho C_p T_{x,y,z;n+1} - dt \cdot \kappa \cdot (\nabla_{r;n+1}^2 T) = \\ \rho C_p T_{x,y,z;n} + dt \cdot S. \end{aligned} \quad (6)$$

To solve the linear system of equations driven from Eq. (6), we could use either analytical or iterative method. We used the iterative generalized minimum residue method,²¹ which saves both computational time and memory for deriving solutions.

Phase Model

As previously assumed in phase models of low-concentrated nanoparticles, we approximate straight light propagation through the sample, with negligible diffraction and refraction effects. Therefore, we assume optical phase changes only, without amplitude changes. In addition, our phase model does not take into account the refractive index of the metal itself, and only considers the refractive index of the medium around the nanoparticles.

Optical phase is proportional to the optical path delay (OPD) of the light interacted with the sample, which is defined as the

product between the refractive index differences and the physical path delay of the light.²² OPD is accumulative across the entire sample thickness, since it accounts for the sum of the differences between the optical routes of the light beam which interacts with the sample, and the reference beam which does not contain spatial sample modulation. In each (x, y) point, OPD as a function of the temperature T is defined by the following equation:

$$OPD(T) = \int L(T) \times n(T) dz, \quad (7)$$

where n is the refractive index of the sample, L is the physical path delay of the light beam, and the integral represents accumulation across the sample thickness. When the temperature changes from T_n to T_{n+1} , both the refractive index and the physical path delay change. Assuming three-dimensional volume expansion due to temperature change, the physical route change in the axial direction can be obtained as followed:

$$L(T_{n+1}) = L(T_n) \times [\rho(T_n)/\rho(T_{n+1})]^{1/3}, \quad (8)$$

where ρ is the solution density.

To assess the change in optical route caused by the surrounding water temperature, we used the dependency of water density ρ (in $[\text{kg}/\text{m}^3]$) on the temperature T (in $[\text{K}]$).²³ By fitting a third degree polynomial curve to thermodynamic tables listing the density of water at different temperatures with R-square = 0.99997, it is found that one can express water density as a function of temperature as follows:

$$\rho(T) = 1.626 \times 10^{-5} T^3 - 1.934 \times 10^{-2} T^2 + 6.957 T + 213.8. \quad (9)$$

The connection between water refractive index n , density of water, and temperature is given in Refs. [24] and [25]. This formulation is based on the Lorentz-Lorenz equation, taking into account molar refraction of water in relation to wavelength, and is fitted to a selected set of accurate refractive index data points measured experimentally, presented as follows:

$$\begin{aligned} \frac{n^2-1}{n^2+2} \left(\frac{1}{\bar{\rho}} \right) = a_0 + a_1 \bar{\rho} + a_2 \bar{T} + a_3 \bar{\lambda}^2 \bar{T} + \\ \frac{a_4}{\bar{\lambda}} + \frac{a_5}{\bar{\lambda}^2 - \bar{\lambda}_{UV}^2} + \frac{a_6}{\bar{\lambda}^2 - \bar{\lambda}_{IR}^2} + a_7 \bar{\rho}^2, \end{aligned} \quad (10)$$

where $\bar{\rho} = \rho/1000$, $\bar{T} = T/273.15$ and $\bar{\lambda} = \lambda/589$, $a_0 = 0.244$, $a_1 = 9.746 \times 10^{-3}$, $a_2 = -3.732 \times 10^{-3}$, $a_3 = 2.687 \times 10^{-4}$, $a_4 = 1.589 \times 10^{-3}$, $a_5 = 2.459 \times 10^{-3}$, $a_6 = 0.9$, $a_7 = -1.666 \times 10^{-2}$, $\bar{\lambda}_{UV} = 229$, and $\bar{\lambda}_{IR} = 5432$.

When working with numerical models rather than analytical solutions, it is possible to handle with nonlinear relations as the relations of temperature to refractive index and of temperature to material density. These nonlinear relations are highly important when trying to understand the dependence of phase-related signals and temperature. Figure 1(a) illustrates the refractive index as a function of temperature for $\lambda = 632.8$ nm (e.g. Helium-Neon laser probing). The dashed green curve describes the linear relation, which was assumed in previous models relating refractive index to temperature.^{11,12,14,26} The solid blue curve describes the nonlinear relation, derived from Eq. (10).

We can see that both linear and nonlinear curves coincide at 25°C such that the linear approximation holds in a limited range of temperatures, whereas for large temperature changes

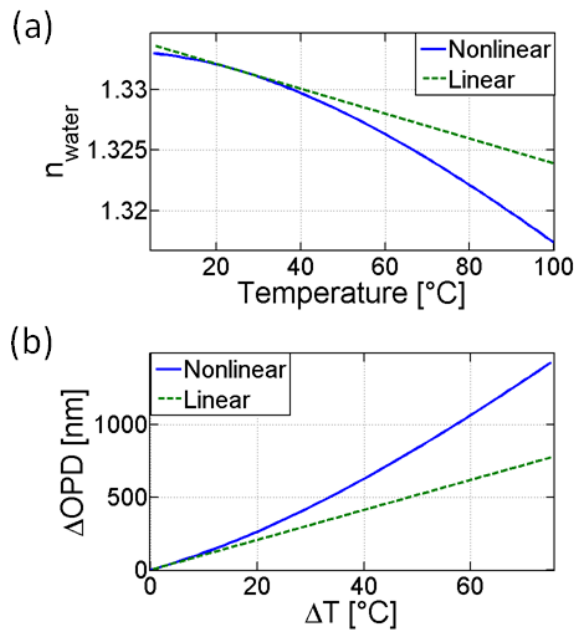


Figure 1 (a) Refractive index of water as a function of temperature according to the linear relation (dashed line), with a starting temperature of 25°C, and according to the nonlinear relation (solid line), both at $\lambda = 632.8$ nm. (b) Change in OPD as a function of the temperature change for a 100 μm water slab, for the linear relation (dashed line), with a starting temperature of 25°C, and for the nonlinear relation (solid line). ΔT is defined as the instantaneous temperature minus the starting temperature. ΔOPD is defined as the OPD at the instantaneous temperature minus the OPD at the starting temperature.

of more than 15 degrees (especially useful for PT therapy), the linear relation fails with a large error. Figure 1(b) describes the computed change in OPD accumulated through a 100 μm water slab as a function of the change in temperature (relative to a starting temperature of 25°C) for the linear and the nonlinear refractive-index to temperature relations. From these graphs, we can see that for heating change of 1 degree, the error in OPD between the linear and non-linear curves is 2%, whereas for 40 degrees, the error increases to 35%. This nonlinear relation affects the phase measurements and induces increasing error for larger temperature changes if applying the inaccurate linear relation used in previous works.

Experimental System

To validate our model experimentally, an optical system was built for acquiring PT phase signals of nanoparticle solutions stimulated photothermally. The PT phase signal is defined as the OPD oscillation magnitude at the temporal frequency of the PT excitation divided by the wavelength and multiplied by 2π . The system, shown in Fig. 2, is based on wide-field interferometric phase microscopy, and is composed of two different light sources: a coherent Helium-Neon (HeNe) laser (100 mW, 632.8 nm) for interferometric imaging, and a diode-pumped solid-state (DPSS) laser, at wavelength of 808 nm, for optical excitation of nanorods. The excitation laser is connected to a waveform generator, which allows temporal modulation of the excitation beam. A dichroic mirror (cut-off wavelength of 700 nm) is used to combine the two laser beams illuminating the sample. The DPSS laser is 1:6 beam expanded using two spherical lenses L0 and L1 (focal lengths of 2.5 cm and 15 cm), and then focused onto the sample using lens L2 with focal length of 40 cm. After the plane-wave imaging beam from the HeNe passes through the sample, it is magnified by a 0.65-NA, 40 \times microscope objective (MV-40X, Newport), and projected on the image plane by spherical tube lens L3 (focal length of 16 cm). A short-pass filter (cut-off wavelength of 700 nm) is positioned after the microscope objective to block the excitation beam from continuing through the imaging channel. The interference is created after the image plane by external off-axis interferometric module. In this module, after splitting the image by slightly tilted beam splitter BS, one beam is optically Fourier transformed using lens L4 (focal length 10 cm), and in the Fourier plane a 30 μm pinhole is positioned in front of a mirror to back reflect only the dc spatial frequency through lens L4 and the beam splitter onto the camera. This configuration effectively erases the sample spatial modulation, and turns this beam into a clear reference beam. In the sample arm of the interferometer, lenses L5 and L6 (focal length of 5 cm each), positioned in a 4f lens configuration, project the sample image onto a slightly tilted mirror, which reflects the beam back to the camera, through the same 4f lens configuration (L5, L6) and the beam splitter. Note that lens L4 focal length is double compared to either lens L5 or lens L6, for optical beam-path matching between the interferometric arms. The reference and sample beams interfere on the camera at a small off-axis angle, which creates an off-axis interferogram on the camera, allowing OPD profile reconstruction from a single camera exposure.²⁷ We used a CCD camera (EPIX 643M), recording

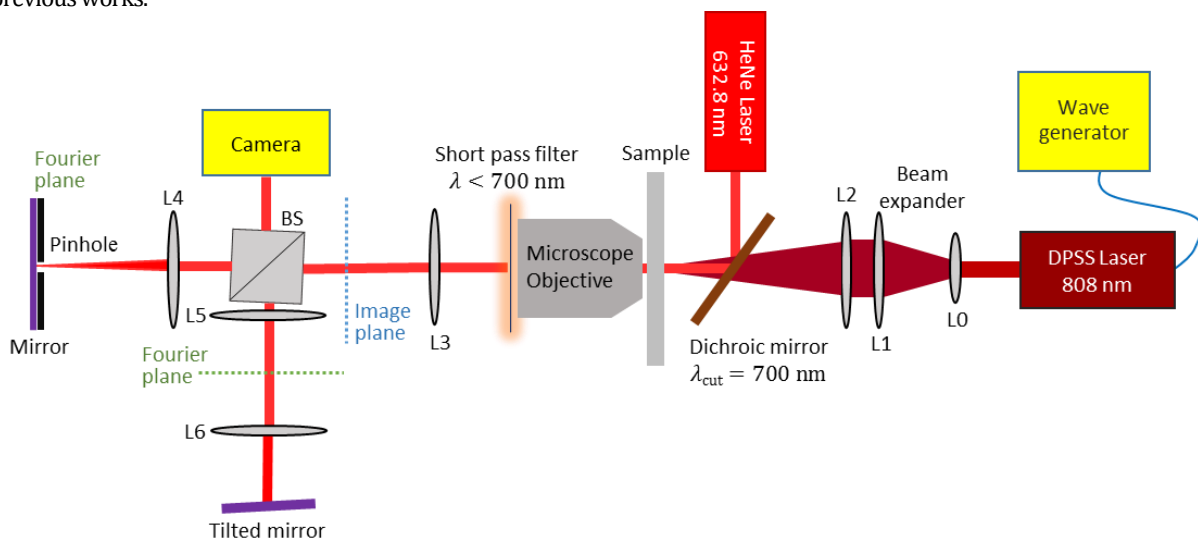


Figure 2 Optical interferometric system scheme used for the experimental measurements.

interferograms of 160×160 pixels at 2 KHz for 2 seconds. Digital reconstruction of the sample OPD is carried out offline using MATLAB software that spatially filters one of the cross-correlation orders resulting after digitally Fourier transforming the recorded off-axis interferogram. This yields the complex wave front of the light transmitted through the sample, containing the sample phase profile, which is proportional to its OPD profile.^{28,29}

RESULTS AND DISCUSSION

Model Demonstrations for Single Nanospheres and Nanorods

To simulate thermal and phase distributions around nanoparticles, we used the heat and phase models described above. To allow reasonable computation time, the size of the grid in the heat model was dependent on the period of observation. For 50 nsec of observation, the voxel size in the grid was 125 nm^3 . For 20 msec of observation, the voxel size in the grid was $1 \mu\text{m}^3$. Totally, the grid contained 6 million points. Since the PT phase signal is modulated in time as a result of the time-modulated excitation, to avoid temperature buildup, per each time point, we created a 3-D dynamic map of the thermal distribution and then observed its temporal dependency. Figure 3 illustrates using the proposed computational model for nanospheres. In this demonstration, we used a gold nanosphere, with $2R = 55 \text{ nm}$ in diameter, absorbing 60 fJ over 5 ns .

The time-modulated intensity of the excitation laser is presented in Fig. 3(a). The resulting thermal distribution 3-D map in Fig. 3(b) shows equal temperature envelopes around the particle at constant temperatures of 20, 10 and $5 \text{ }^\circ\text{C}$ above the starting temperature of $25 \text{ }^\circ\text{C}$. Per each time point, two-dimensional OPD maps are extracted from the thermal distribution, by accumulation along the Z axis using Eq. (7). This 2-D map is shown in Fig. 3(c), where the maximal OPD at time 5 ns is 0.056 nm (see entire dynamics is Video 1). Figure 1(d) shows two oscillating OPD signals, the first one at the particle center (solid line), and the second one at a distance R from the particle center (dashed line). Figure 1(e) shows the Fourier power spectrum of the time-modulated signals shown in Fig. 1(d), after reducing a quadratic fit from the temporal signals, to neglect the temperature buildup overtime.¹⁴

Next, we verified results from our model for a $2R=50 \text{ nm}$ gold nanosphere stimulated with a CW laser excitation. The numerical simulation generated a heat distribution map for the particle and its environment during 300 ns of constant excitation, with a starting room temperature of 25°C . Figure 4(a) shows the dependency of temperature in time for various ratios between the distances from the nanosphere center r and the nanosphere radius R . These results correlate well with previous finite element models of heat conduction.⁷

One of the advantages of the presented model compared to the previous ones is the possibility of analyzing thermal and phase signatures of arbitrary shaped nanoparticles including semi-symmetric and even non-symmetric shapes, and not only spheres. Figure 5(a) shows simulation of the thermal and OPD distributions due to time-modulated excitation of a nanorod $55 \times 150 \text{ nm}$ in diameters (Fig. 5(a), and Video 2 for the full dynamics), a nanocube, $55 \times 55 \times 55 \text{ nm}$ in size (Fig. 5(b), and Video 3 for the full dynamics), and a nanocage $55 \times 55 \times 55 \text{ nm}$ in size, with edge

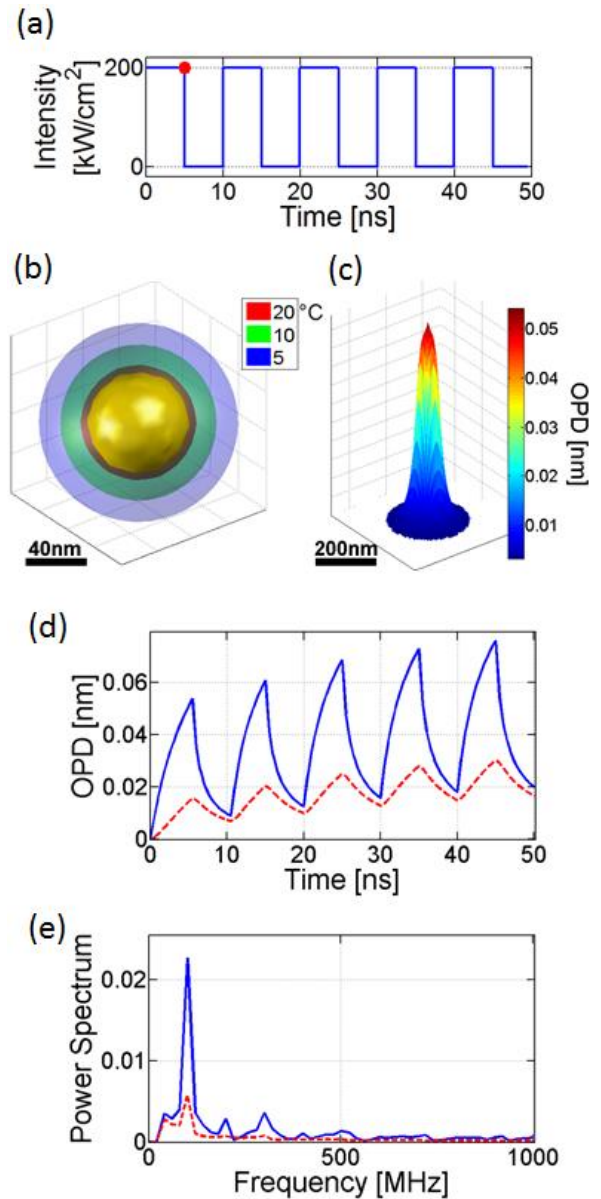


Figure 3 Demonstration of using the proposed model for simulating the thermal and OPD distributions of a single nanosphere, $2R = 55 \text{ nm}$ in diameter, absorbing 300 fJ over 50 ns . **(a)** The intensity of the excitation laser on the sample as a function of time, with excitation frequency of 100 MHz . **(b)** Thermal distribution 3-D map resulting 5 ns after the excitation starts, at the red point marked in Fig. 3(a). **(c)** The coinciding OPD map. See the full dynamics in Video 1. **(d)** OPD at the central location of the nanosphere (solid-line graph) and at a distance R from the center of the nanoparticle (dashed-line graph) as a function of time. **(e)** The coinciding power spectrums.

thickness of 10 nm (Fig. 5(c), and Video 4 for the full dynamics).

As can be seen in these figures and videos, surfaces depicting identical temperatures create different geometrical shapes depending on the distance from particle surface. Close to the particles (i.e. red envelopes), the equi-temperature surfaces resemble the particle shape, whereas farther from the particles (i.e. blue envelopes), the equi-temperature surfaces resemble a sphere shape. Therefore, the behavior of the associated phase map measured close to the particle can imply on the material, shape and size of the nanoparticle, as was previously suggested.³⁰

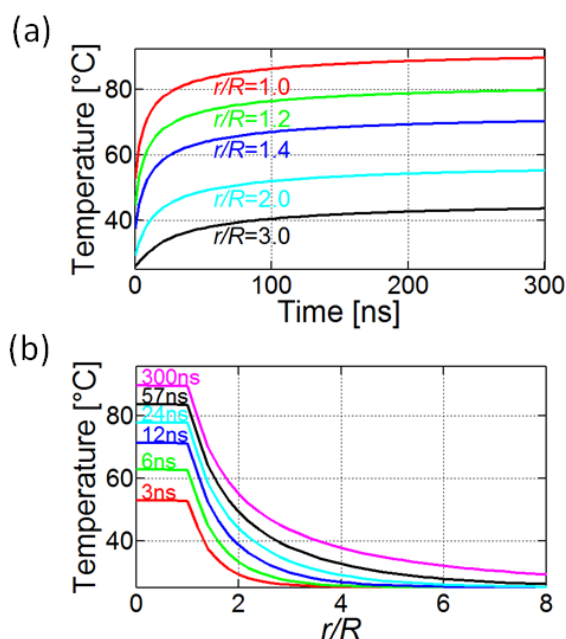


Figure 4 Thermal temporal and spatial dependencies for a $2R = 50$ nm gold nanosphere. **(a)** Temperature as a function of time for various distances r from the particle center. **(b)** Temperature as a function of the ratio between the distance from the particle center r and the radius of the particle R for various times.

In addition to changing the nanoparticle shape, the proposed model can be used to calculate the thermal and OPD distributions around arbitrary number of nanoparticles located at arbitrary locations. For example, Fig. 6 and Videos 5-7 present the thermal and OPD distributions due to time-modulated excitation for two, three and four gold nanorods. As can be seen in the two latter cases, a new mutual OPD peak is built with time in the central location between the particles (see at the end of Videos 6 and 7) due to temperature buildup.

Correlation with Experimental Results for Nanorod Solution

The wide-field interferometric phase microscopy system presented in Fig. 2 and Section 3 was built for measuring PT phase signals of nanoparticle solutions. The measurements conducted were used to verify our computational model.

Simulative and experimental data were taken for 10×40 nm gold nanorods at peak resonance wavelength of 808 nm, excitation power range of 0 – 100 mW, excitation frequency range of 70 – 1000 Hz, and solution concentration range of 3×10^{10} – 53×10^{10} particles/ml. The measurements were done by diluting a nanoparticle solution in a 100 μm deep silicon well of deionized water. PT excitation of the solution stimulated nanoparticle heat absorption, following phase change, which was not present in the pure water measurements.

In the simulations, nanoparticle excitation power and laser beam shape were considered to resemble the experimental optical system setup. Simulation and experimental results representing the spatially averaged PT phase signal across a field of view of 160×160 pixels, as a function of the excitation laser power are shown in Fig. 7(a). As expected, an increase in the excitation laser power intensifies the PT phase signal originating from the nanoparticle solution. However, in contrast to results from previous researches,^{14,26} we observed a nonlinear relation between

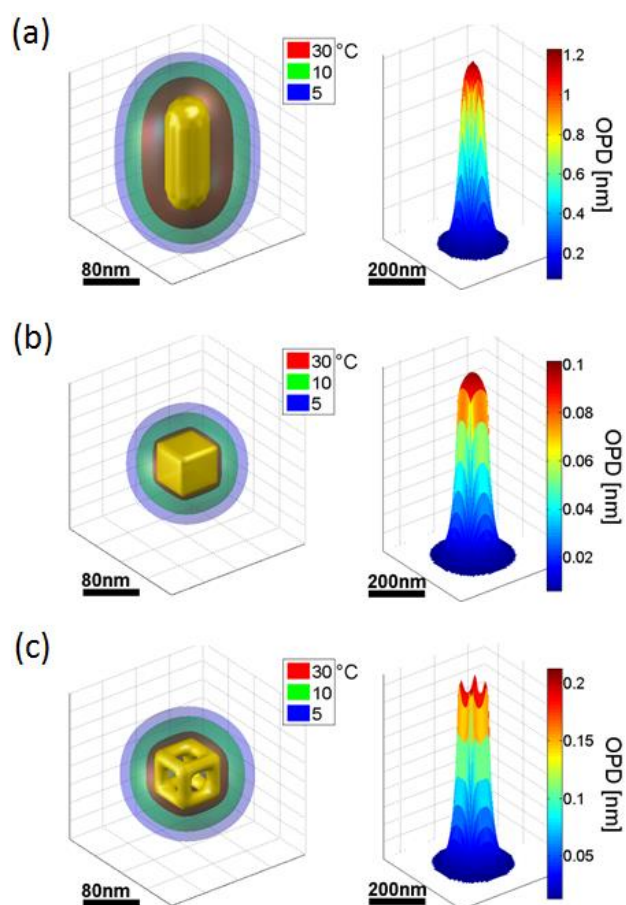


Figure 5 Demonstration of using the proposed model for simulating the thermal and OPD distributions of various gold nanoparticle shapes. **(a)** Thermal and OPD distributions around a nanorod, 55×150 nm in diameters, absorbing 260 fJ, 5 ns after the excitation starts, at the red point marked in Fig. 3(a). See the full dynamics in Video 2. **(b)** Thermal and OPD distributions around a nanocube, $55 \times 55 \times 55$ nm in sizes, absorbing 120 fJ, 5 ns after the excitation starts, at the red point marked in Fig. 3(a). See the full dynamics in Video 3. **(c)** Thermal and OPD distributions around a nanocage, $55 \times 55 \times 55$ nm in sizes with edge thickness of 10 nm, absorbing 333 fJ, 5 ns after the excitation starts, at the red point marked in Fig. 3(a). See the full dynamics in Video 4.

the averaged PT phase signal and the excitation power. This can be explained by the nonlinear relation of phase change to medium temperature. As seen in Fig. 7(a), good correlation was obtained between the simulation results of the proposed model and the experimental results measured by the optical system illustrated in Fig. 2.

Figure 7(b) presents simulation and experimental results of the spatially averaged PT phase signal as a function of the excitation-laser modulation frequency. The excitation modulation frequency and the pulse duty cycle affect both the nanoparticle maximum temperature and the phase oscillation magnitude. As seen in Fig. 7(b), good agreement was achieved between the model simulation results and the experimental measurements obtained by the optical system illustrated in Fig. 2. Increasing excitation frequency reduces the heat-cool cycle time, the phase-signal amplitude, and ultimately the PT phase signal originating from each particle. Change of heat-cool cycle time also affects the thermal diffusion radius, such that higher excitation frequency

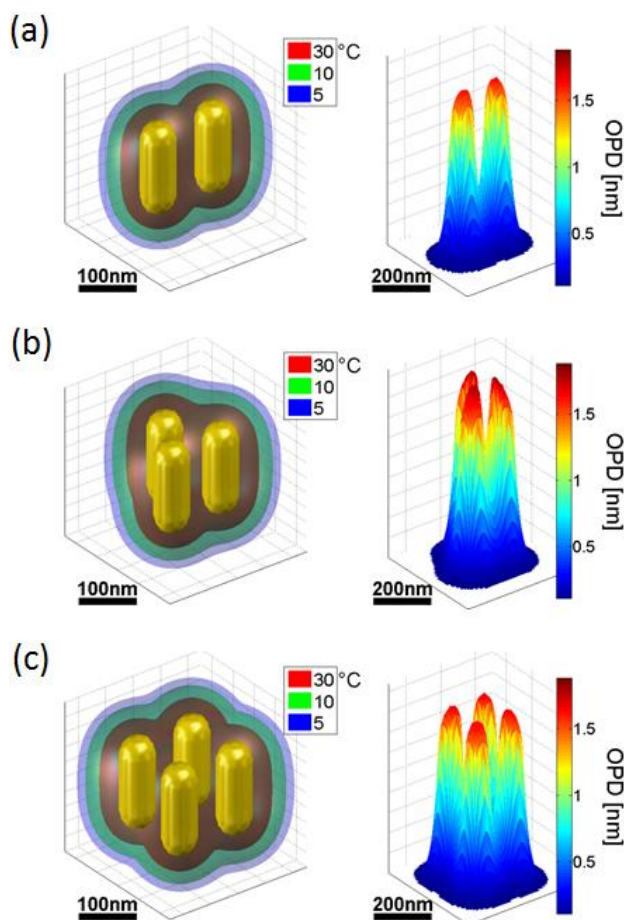


Figure 6 Demonstration of using the proposed model for simulating the thermal and phase distributions of multiple particles together. We used nanorods, each of which is 55×150 nm in diameters and absorbs 260 fJ, 5 ns after the excitation starts, at the red point marked in Fig. 3(a). Thermal and OPD distributions of: **(a)** Two nanorods. **(b)** Three nanorods. **(c)** Four nanorods.

results in smaller diffusion radius, making the thermal disturbance more confined. This, in turn, causes the phase signal to reduce in diameter, which can be observed by using fast imaging techniques for detection of phase changes, where one can see the spread of thermal disturbance as a function of time.³¹ This reduction in PT phase signal diameter allows for easier distinction between adjacent particles but also reduces the PT phase signal strength.

Figure 7(c) shows comparison between simulation results obtained by the proposed model and experimental results obtained by the optical system illustrated in Fig. 2, for the dependency of the spatially averaged PT phase signal and the nanoparticle concentration, again with good correlation between these results. As seen in these graphs, the nanoparticle concentration within solution affects the optical cross-section for energy absorbance and the proximity of individual nanoparticles. Higher concentration of particles induce stronger PT phase signal in a nonlinear manner. This nonlinearity is mostly due to nanoparticle thermal envelope integration causing a nonlinear effect that grows with particle proximity. This means that the increase in signal is due to both the linearly increasing cross-section of the nanoparticle and the nonlinear dependency of phase and temperature. This nonlinear effect might be used in the future for proximity measurements of particles on the Z axis, since when

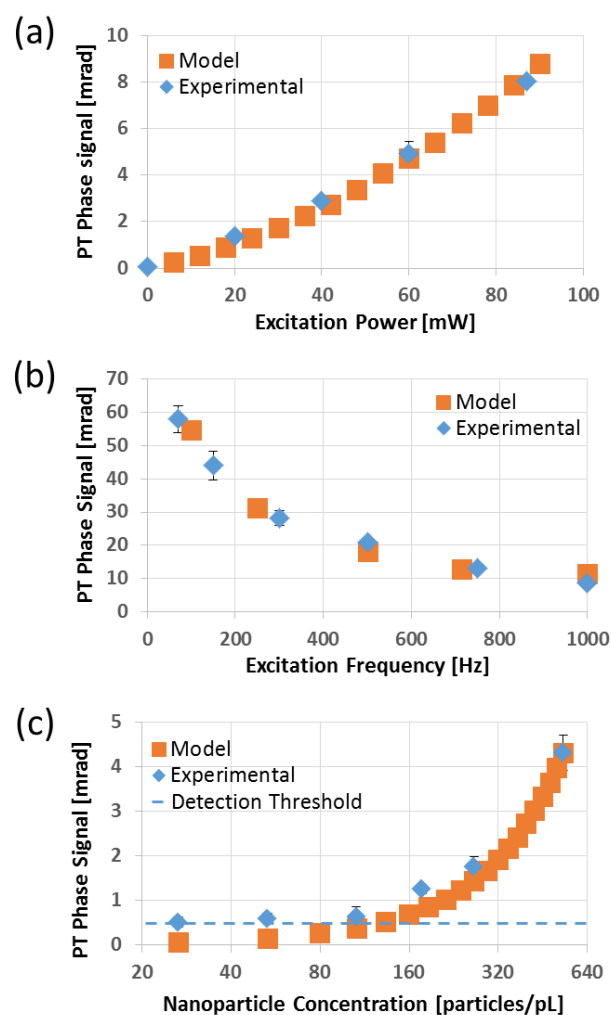


Figure 7 Comparison between the results obtained by the proposed model and experimental results for a solution of gold nanorods. **(a)** Spatially averaged PT phase signal as a function of excitation power ($R^2=0.991$ correlation between the graphs). **(b)** Spatially averaged PT phase signal as a function of excitation laser frequency at duty cycle of 50% ($R^2=0.987$ correlation between the graphs). **(c)** Spatially averaged PT phase signal as a function of nanoparticle concentration ($R^2=0.93$ correlation between the graphs).

two particles get closer, the PT phase signal emitted increases.

The experimental detection threshold is shown in Fig. 7(c) as a dashed horizontal line. Most importantly, the proposed model can deduce PT phase signals even for concentrations which are below the detection threshold of the experimental system.

CONCLUSIONS

We have presented a new computational model that can numerically calculate thermal distribution maps around arbitrary shaped nanoparticles excited photothermally, and find the coinciding phase maps of light that would be transmitted through the sample. These particles are typically used in the sample to obtain imaging contrast or for therapy by heating. The presented model can be used to optimize various parameters of the nanoparticles and their excitation prior to the actual experiment. We have correlated simulation results obtained by using our model to both previous thermal distribution studies of plasmonic nanoparticles and new experimental results obtained by a wide-field interferometric phase microscopy. Our results show good

agreement for various parameters including the nanoparticle size and concentration, the excitation frequency, and the resulting PT phase profiles. These results confirm that the new nonlinear computational model presented can be used for the optimization of nanoparticles prior to their synthesis, as well as for investigation of nanoparticle processes and surface interactions by their phase signatures. Thus, the presented tool can improve detection efficiency of phase-sensitive techniques that use nanoparticles by optimizing the optical setup parameters, the excitation parameters, and the particle parameters. In addition, using our model together with prior knowledge on the absorbers used, one can potentially measure far-field phase profiles and estimate heat distribution on and around the nanoparticle.

REFERENCES

- Link S, El-Sayed MA. Shape and size dependence of radiative, non-radiative and photothermal properties of gold nanocrystals. *Int Rev Phys Chem* 2000; **19**: 409–453.
- Huang X, El-Sayed MA. Plasmonic photo-thermal therapy (PPTT). *Alexandria J Med* 2011; **47**: 1–9.
- Huang X, Jain PK, El-Sayed IH, El-Sayed MA. Determination of the minimum temperature required for selective photothermal destruction of cancer cells with the use of immunotargeted gold nanoparticles. *Photochem Photobiol* 2006; **82**, 412–417.
- Fixler D, Zalevsky Z. In vivo tumor detection using polarization and wavelength reflection characteristics of gold nanorods. *Nano Lett* 2013; **13**, 6292–6296.
- Richardson HH, Carlson MT, Tandler PJ, Hernandez P, Govorov AO. Experimental and theoretical studies of light-to-heat conversion and collective heating effects in metal nanoparticle solutions. *Nano Lett* 2009; **9**, 1139–1146.
- Volkov AN, Sevilla C, Zhigilev LV. Numerical modeling of short pulse laser interaction with Au nanoparticle surrounded by water. *Appl Surf Science* 2007; **253**, 6394–6399.
- Sassaroli E, Li KCP, O'Neill BE. Numerical investigation of heating of a gold nanoparticle and the surrounding microenvironment by nanosecond laser pulses for nanomedicine applications. *Phys Med Biol* 2009; **54**, 5541–5560.
- Ekici O, Harrison RK, Durr NJ, Eversole DS, Lee M, Ben-Yakar A. Thermal analysis of gold nanorods heated with femtosecond laser pulses. *J Phys D Appl Phys* 2008; **41**, 185501.
- Au L, Zheng D, Zhou F, Li ZY, Li X, Xia YA. Quantitative study on the photothermal effect of immuno gold nanocages targeted to breast cancer. *ACS Nano* 2008; **2**, 1645–1652.
- Huang X, El-Sayed IH, Qian W, El-Sayed MA. Cancer cell imaging and photothermal therapy in the near-infrared region by using gold nanorods. *J Am Chem Soc* 2006; **128**, 2115–2120.
- Cognet L, Tardin C, Boyer D, Choquet D, Tamarat P, Lounis B. Single metallic nanoparticle imaging for protein detection in cells. *Proc Natl Acad Sci* 2003; **100**, 11350–11355.
- Boyer D, Tamarat P, Maali A, Lounis B, Orrit M. Photothermal imaging of nanometer-sized metal particles among scatterers. *Science* 2002; **297**, 1160–1163.
- Skala MC, Crow MJ, Wax A, Izatt JA. Photothermal optical coherence tomography of epidermal growth factor receptor in live cells using immunotargeted gold nanospheres. *Nano Lett* 2008; **8**, 3461–3467.
- Adler DC, Huang SW, Huber R, Fujimoto JG. Photothermal detection of gold nanoparticles using phase-sensitive optical coherence tomography. *Opt Express* 2008; **16**, 4376–4393.
- Turko NA, Peled A, Shaked NT. Wide-Field interferometric phase microscopy with molecular specificity using plasmonic nanoparticles. *J Biomed Opt* 2013; **18**, 111414.
- Dewhirst MW, Viglianti BL, Lora-Michiels M, Hanson M, Hoopes PJ. Basic principles of thermal dosimetry and thermal thresholds for tissue damage from hyperthermia. *Int J Hyperthermia* 2003; **19**, 267–294.
- Huang X, Kang B, Qian W, Mackey MA, Chen PC, Oyeler AK, El-Sayed IH, El-Sayed MA. Comparative study of photothermolysis of cancer cells with nuclear-targeted or cytoplasm-targeted gold nanospheres: continuous wave or pulsed lasers. *J Biomed Opt* 2010; **15**, 058002.
- Link S, Mohamed MB, El-Sayed MA. Simulation of the optical absorption spectra of gold nanorods as a function of their aspect ratio and the effect of the medium dielectric constant. *J Phys Chem B* 1999; **103**, 3073–3077.
- Recktenwald GW. Finite-difference approximations to the heat equation. *CI Notes* 2004.
- Hoffman JD, Frankel S. *Numerical Methods for Engineers and Scientists*. New York: CRC press, 2001: 270–279.
- Saad Y, Schultz MH. GMRES: A generalized minimal residual algorithm for solving nonsymmetric linear systems. *SIAM J Sci Stat Comput* 1986; **7**, 856–869.
- Murphy DB, Davidson MW. *Fundamentals of Light Microscopy and Electronic Imaging*. New Jersey: John Wiley & Sons, 2012.
- Moran MJ, Shapiro HN, Boettner DD, Bailey MB. *Fundamentals of Engineering Thermodynamics*. New Jersey: John Wiley & Sons, 2010: 817–818.
- Schiebener P, Straub J, Sengers JL, Gallagher JS. Refractive index of water and steam as function of wavelength, temperature and density. *J Phys Chem Ref Data* 1990; **19**, 677–717.
- Harvey AH, Gallagher JS, Sengers JL. Revised formulation for the refractive index of water and steam as a function of wavelength, temperature and density. *J Phys Chem Ref Data* 1998; **27**, 761–774.
- Tucker-Schwartz JM, Meyer TA, Patil CA, Duvall CL, Skala MC. In vivo photothermal optical coherence tomography of gold nanorod contrast agents. *Biomed Opt Express* 2012; **3**, 2881–2895.
- Cuche E, Marquet P, Depeursinge C. Simultaneous amplitude-contrast and quantitative phase-contrast microscopy by numerical reconstruction of Fresnel off-axis holograms. *Appl Opt* 1999; **38**, 6994–7001.
- Herráez MA, Burton DR, Lalor MJ, Gdeisat MA. Fast two-dimensional phase-unwrapping algorithm based on sorting by reliability following a noncontinuous path. *Appl Opt* 2002; **41**, 7437–7444.
- Girshovitz P, Shaked NT. Real-time quantitative phase reconstruction in off-axis digital holography using multiplexing. *Opt Lett* 2014; **39**, 2262–2265.
- Baffou G, Quidant R, García de Abajo F. J. Nanoscale control of optical heating in complex plasmonic systems. *ACS Nano* 2010; **4**, 709–716.
- Zharov VP, Lapotko DO. Photothermal imaging of nanoparticles and cells. *IEEE J Sel Top Quantum Electron* 2005; **11**, 733–751.